

Article

Design and Analysis of Outer Rotor Permanent-Magnet Vernier Machines with Overhang Structure for In-Wheel Direct-Drive Application

Dong Yu , Xiaoyan Huang *, Lijian Wu and Youtong Fang

College of Electrical Engineering, Zhejiang University, Hangzhou 310027, China; 11410025@zju.edu.cn (D.Y.); lijianwu@zju.edu.cn (L.W.); youtong@zju.edu.cn (Y.F.)

* Correspondence: xiaoyanhuang@zju.edu.cn; Tel.: +86-8795-3134

Received: 26 February 2019; Accepted: 28 March 2019; Published: 1 April 2019



Abstract: This paper presents a novel outer rotor permanent-magnet vernier machine (PMVM) for in-wheel direct-drive application. The overhang structures of the rotor and flux modulation pole (FMP) are introduced. The soft magnetic composite (SMC) was adopted in the FMP overhang to allow more axial flux. The 3-D finite element analysis (FEA) was carried out to prove that the proposed machine can effectively utilize the end winding space to enhance the air-gap flux density. Hence the PMVM can offer 27.3% and 14.5% higher torque density than the conventional machine with no overhang structure and the machine with only rotor overhang structure, respectively. Nevertheless, the efficiency of the proposed machine is slightly lower than the conventional ones due to the extra losses from the overhang structures.

Keywords: permanent-magnet vernier machine; in-wheel direct-drive; outer rotor; overhang; soft magnetic composite

1. Introduction

The vernier machine was first proposed in the form of the vernier reluctance machine without any attention at that time [1]. Then, with the rapid development of the permanent magnet (PM) materials, the permanent-magnet vernier machine (PMVM) has been highlighted in recent years in various applications requiring high torque and power density, such as the in-wheel direct-drive system for the electric vehicle (EV) [2–6]. The PMVM can effectively utilize the magnetic flux harmonics to achieve higher output torque at a low speed due to the “magnetic gearing effect”. Nevertheless, a relatively poor power factor (PF) is inevitable because of its inherent nature. Thus, an inverter with higher power rating is required, which will increase the size and cost of the whole system. The 3-D finite element analysis (FEA) and experiment results indicated that by replacing the surface-mounted PM with the spoke-type PM, the output torque capability and PF of the PMVMs can be significantly improved [7–10]. In addition, the PMVM with concentrated winding and the multitooth flux modulation poles (FMPs) can effectively shorten the length of the end winding, reduce the copper loss, and consequently improve the efficiency of the machine [11–14].

The PMVM with only the rotor overhang structure received more attention recently for applications with limited space in axial direction. By utilizing the end winding space, the rotor overhang structure can enhance the air-gap flux density and therefore the torque density. Both the analytical method and the finite element method (FEM) were carried out to analyze the effect of this structure [15–18]. Nevertheless, the conventional overhang structures only increase the axial stack length of the rotor. The effect could be compromised when the FMP remains the same as in the conventional design.

In this paper, a novel outer rotor PMVM with the overhang structure of the rotor and FMP will be proposed for the in-wheel direct-drive application. In Section 2, the operation principle and topology of the proposed machine are introduced. In Section 3, 3-D FEM simulations are carried out to verify the design of the proposed machine structure.

2. Operation Principle and Machine Configurations

The modulation principle is based on the “magnetic gearing effect”, which means that a low-speed rotation of the PMs will cause dramatic variations in flux. Furthermore, the flux will interact with the high-speed rotating field generated by armature windings to produce the torque [19,20]. The FMPs are the key to cause these two rotating fields’ modulation in a PMVM. To take advantage of the magnetic gearing effect, the number of FMPs (Z_s), the armature winding fundamental pole pair (p_s), and the PM pole pair (p_r) should meet the following equation:

$$p_r = Z_s \pm p_s \quad (1)$$

Figure 1 shows the configurations of the three PMVMs, M I, M II, and the proposed M III. All of them have the outer rotor structure and surface-mounted PMs. Each machine has the same Z_s , p_r , and p_s combination of 36/28/8 and their stator teeth are split into two FMPs, which makes the stator feasible to adopt concentrated winding to shorten the length of end winding. The double-layer concentrated windings with Y connection were applied in this design as shown in Figure 1g. In order to transmit torque at different speeds, the fundamental space harmonics velocity in the stator should be G_r times higher than that in the rotor, which is

$$G_r = \frac{\omega_s}{\omega_r} = \frac{p_s - Z_s}{p_s} \quad (2)$$

where ω_s and ω_r are the stator and rotor magnetic field rotating speeds, respectively.

The M II PMVM with the 10 mm bilateral rotor overhang structure is shown in Figure 1b. The length of overhang is determined according to the length of end winding. Apart from the difference in rotor, the stator of M II is also optimized for high torque density; the main differences are listed in Table 1.

In the proposed M III PMVM, both rotor overhang and FMP overhang are implemented to maximize the output torque. The FMPs have the same length of the rotor with overhang structure to provide the shortcut for the flux from the rotor overhang to the stator. Moreover, the FMPs of the proposed machine are partitioned from the stator to reduce the losses and cost of the SMC as shown in Figure 1c–f.

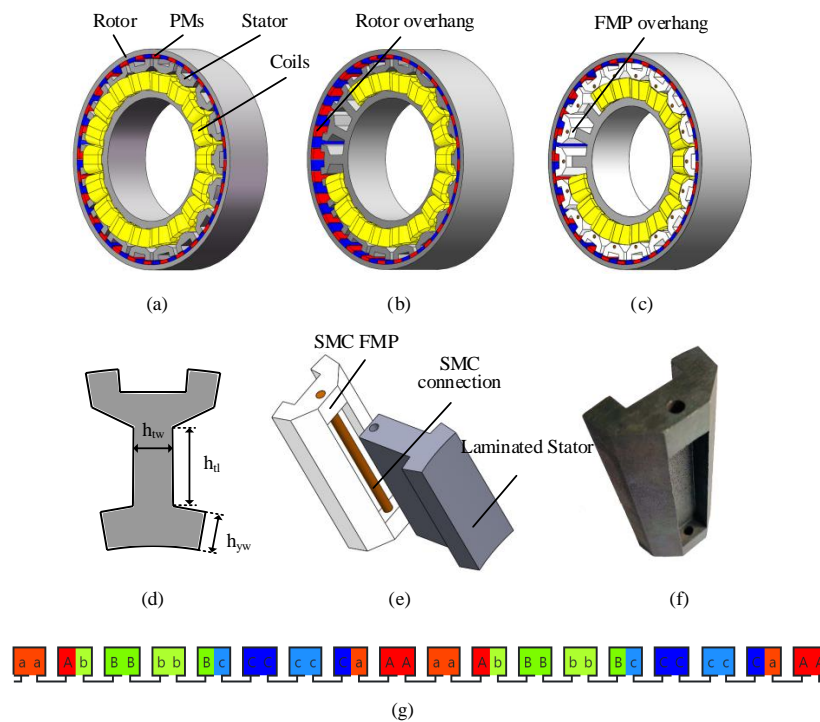


Figure 1. The configurations of the three machines. (a) M I: conventional PMVM. (b) M II: PMVM with rotor overhang. (c) M III: proposed PMVM with rotor and FMP overhang. (d) Cross-section of conventional stator tooth. (e) Side view of the proposed stator tooth. (f) FMP prototype. (g) Winding configuration.

Table 1. Main specifications of the three machines.

Parameters	M I	M II	M III
Number of stator slots		18	
Number of FMPs		36	
Number of rotor pole pairs		28	
Number of winding pole pairs		8	
Gear ratio		−28:8	
Rotor outer diameter (mm)		250	
Stator outer diameter (mm)		228	
Stator inner diameter (mm)	140	134	128
Air-gap length (mm)		1	
PM width (mm)		12	
PM thick (mm)		4	
Rotor axial length (mm)	60	80	80
Stator axial length (mm)	60	60	60
FMP axial length (mm)	60	60	80
Stator tooth width h_{tw} (mm)	10.0	11.5	13.0
Stator tooth length h_d (mm)	20.3	22.5	24.4
Stator yoke width h_{yw} (mm)	8.0	9.0	10.0
Stator and rotor material		50ww350	
FMP material	50ww350	50ww350	Somaloy700
PM material	NdFeB38EH	NdFeB38EH	NdFeB38EH
Rated speed (rpm)		600	
Rated current (A)		20	
Current density (A/mm ²)		5	
Slot packing factor		0.6	
Turns per slot		40	
Winding resistance (Ω)		0.088	

The back electromotive force (EMF) and rated load torque increase versus overhang length of M II and M III are shown in Figure 2. It should be noted that when the length of the overhang is under 2 mm, the M II produces higher back EMF and torque than the M III. There are mainly two reasons: one is that when the overhang is short, the air-gap reluctance and the flux leakage of the rotor overhang is relatively small; and the other one is that the permeability of SMC is slightly smaller than the silicon steel as shown in Figure 3. As the length of the overhang increases, the flux linkage must pass through a longer air gap which mitigates the increased air-gap flux density. When the rotor overhang is long enough, the advantage of the proposed structure becomes obvious. The additional FMP overhang can effectively utilize the rotor overhang, which produces higher back EMF and torque in comparison with M II. Since the length of end winding of the machine is around 10.8 mm, a 10 mm overhang length is selected for M II and M III. In addition, the dimension of the stator is optimized for M II and M III to avoid saturation in the stator teeth while maintaining the same current density. Main parameters of the three PMVMs are summarized in Table 1.

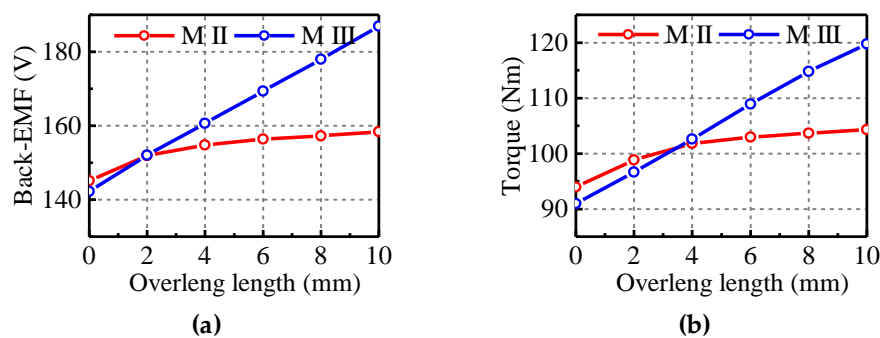


Figure 2. Back EMF (a) and torque (b) versus overhang length of M II and M III.

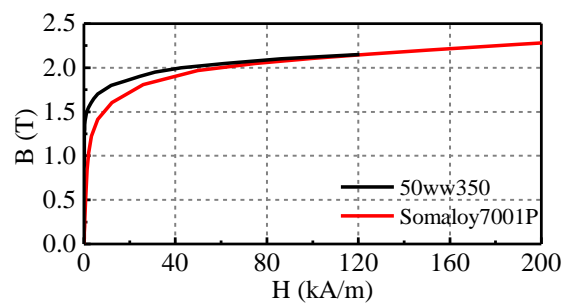


Figure 3. B–H curve of silicon steel and SMC.

3. FEA and Comparisons

As the overhang structure causes asymmetry in the axial direction, the 3-D FEM is essential for further analysis.

3.1. No-Load Characteristics

The no-load back EMF waveforms and their harmonic distributions of the three machines at the rotor speed of 600 rpm are demonstrated and compared in Figure 4. It can be seen that the back EMF amplitude of the proposed M III is the highest, 28.8% and 18.0% higher than the M I and the M II, respectively.

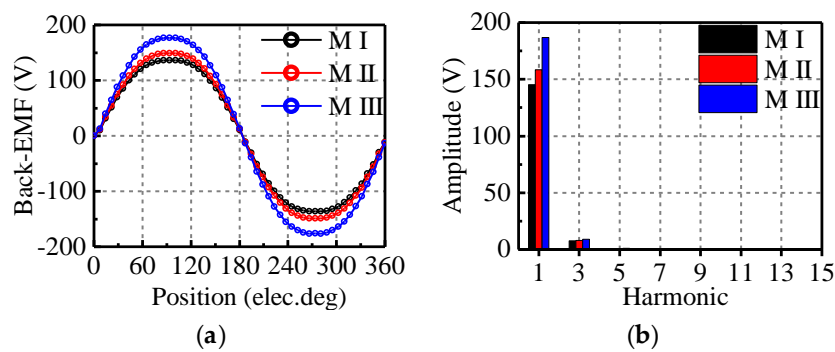


Figure 4. No-load back EMF of the three machines at 600 rpm. (a) Waveform. (b) Harmonic distributions.

The radial component of the air-gap flux density at the axial position of 0 mm and the corresponding space harmonic spectrum are shown in Figure 5a and c. In addition, the air-gap flux densities of M I and M II at the axial 0 mm position (the middle of the machines) are the same and the 28th harmonic orders are slightly higher than the M III's. This is mainly because of the low permeability of SMC applied to the FMPs, and this also could lead to the difference of back EMF between M II and M III when the overhang length is 0 mm as shown in Figure 2. The amplitude of the 28th harmonic order of air-gap flux density versus axial position are compared in Figure 5b. It should be noted that the air-gap flux density of M II drops apparently at the axial position near the rotor overhang, which is between 30 mm to 40 mm and -30 mm to -40 mm. However, the proposed M III can keep the high air-gap flux density until it reaches the edge of the overhang. As shown in Figure 6a, the PM flux linkage of the rotor overhang passes through the air gap and goes into the stator and contributes to the main flux linkage. However, this effect could be mitigated when the length of the overhang is increasing, and this problem is overcome by adding the FMP overhang. The flux linkage of the rotor overhang can successfully pass into the FMP overhang and then into the stator, in which way the reluctance is much smaller than the M II's, and less flux leakage occurs as shown in Figure 6b. Meanwhile, this also benefits from the SMC, which allows more axial flux. Therefore, the air-gap flux density of M III is improved, which contributes to the increase of back EMF and output torque.

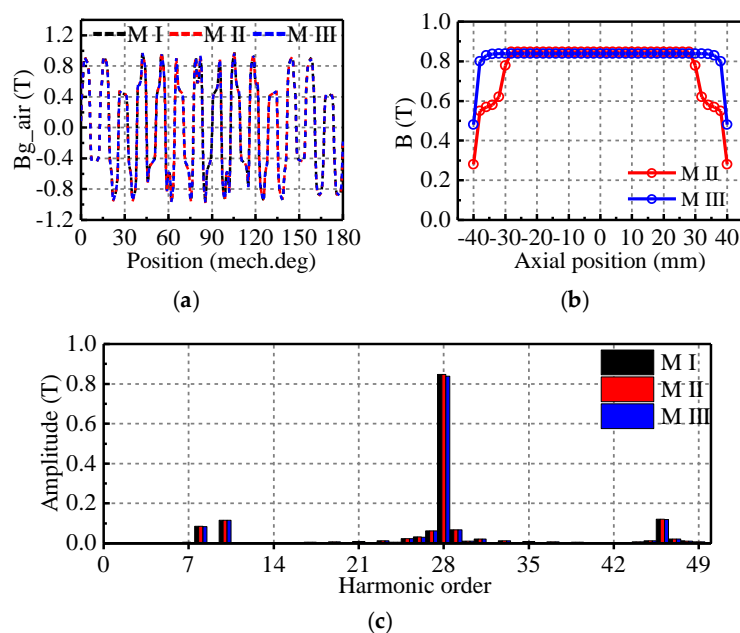


Figure 5. No-load air-gap magnetic flux density. (a) 0 mm waveform. (b) Air-gap flux density versus axial position. (c) 0 mm harmonic distributions.

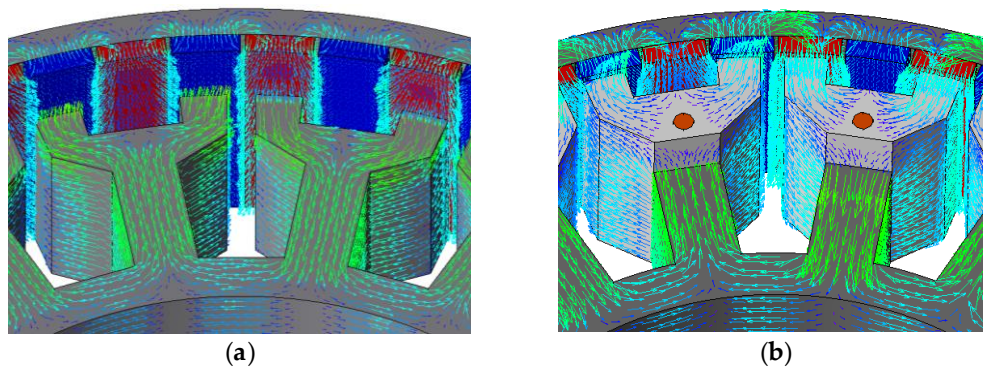


Figure 6. 3D magnetic flux density vector diagram at no-load condition. (a) M II. (b) M III.

3.2. On-Load Characteristics

The flux density distributions of the three PMVMs at the rated load (20 Arms current with $i_d = 0$ control) are compared in Figure 7. It can be seen that through the stator size adjustment, the maximum flux density in stator teeth of all the three machines are about 1.7 T, which is a typical value for the silicon steel 50ww350.

The characteristics of the three PMVMs at rated load condition are summarized in Table 2. The output waveforms of the three PMVMs at the rated load condition are shown in Figure 8. The proposed M III can offer higher output torque and power, which is 27.3% higher than M I and 14.5% higher than M II. The torque ripple of all the three machines is relatively low without any additional torque ripple reduction technique adopted, which is 1.52 Nm (1.6%), 1.70 Nm (1.8%), and 1.47 Nm (1.5%), respectively. The total weight (including stator, rotor, PMs, winding, and shell) and volume of the three machines are also calculated, and M III has the highest torque density in terms of Nm/kg and Nm/L.

Table 2. Main rated load performance of the three machines.

Items	M I	M II	M III
Average torque (Nm)	94.0	104.5	119.7
Torque ripple (Nm)	1.52 (1.6%)	1.70 (1.8%)	1.47 (1.5%)
Power (kW)	5.90	6.56	7.52
Loss (W)	412.4	442.2	572.5
Efficiency	93.5%	93.7%	92.9%
Weight (kg)	12.88	14.86	15.76
Torque density (Nm/kg)	7.30	7.03	7.60
Volume (L)	5.54	5.54	5.54
Torque density (Nm/L)	16.97	18.86	21.61

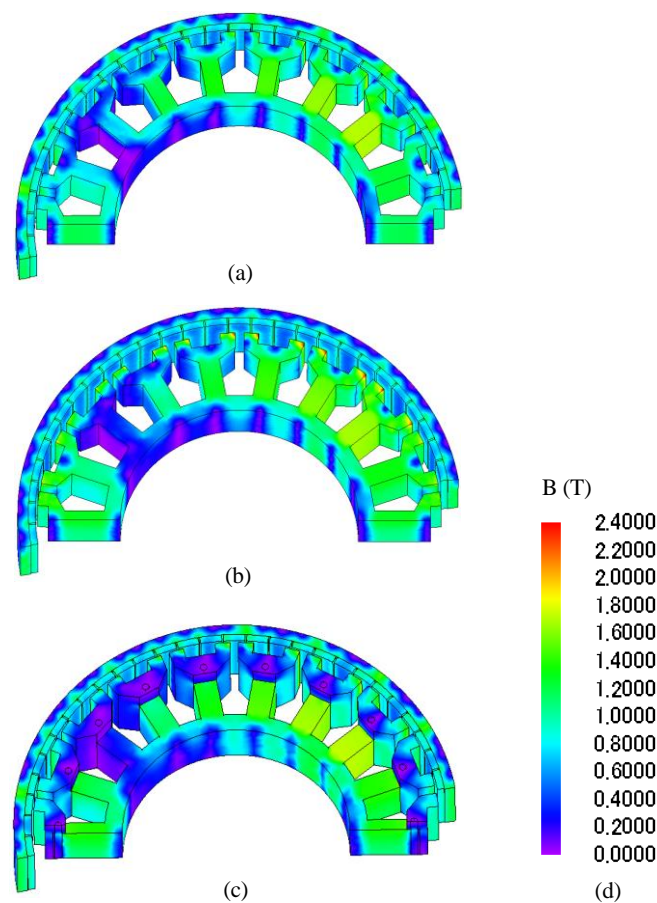


Figure 7. Flux density distributions of the three machines at rated load condition. (a) M I. (b) M II. (c) M III. (d) Scale bar.

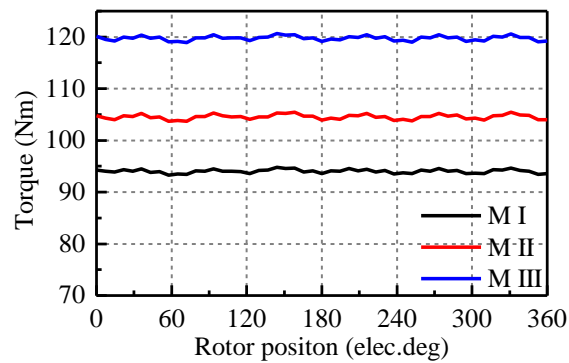


Figure 8. Output torque waveforms of the machines at rated load condition.

The main losses of the three PMVMs at rated load condition are listed in Figure 9. The copper loss of the three PMVMs is almost the same. The PM eddy current loss of these PMVMs cannot be neglected due to the high frequency. The losses in the rotor cores are very small while the stator core losses dominate. The efficiency of the three PMVMs can be approximated as

$$\eta = \frac{P_o}{P_o + P_{loss}} \quad (3)$$

where P_o is the output power and P_{loss} are the losses listed in Figure 9.

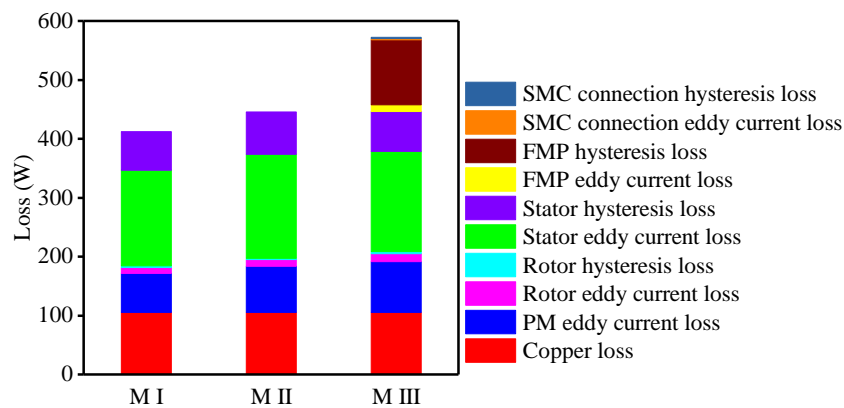


Figure 9. On-load loss comparison of the three PMVMs.

However, the hysteresis loss of the FMPs of M III is relatively high due to SMC inherent material characteristics, which lead to the increase of total loss. Besides the higher cost and relatively higher hysteresis loss of SMC material, only FMPs are made of SMC and the other parts of the stator cores are made of laminations in this paper.

4. Conclusions

In this paper, a novel outer rotor PMVM for in-wheel direct-drive application has been proposed, in which the overhang structure of the rotor and FMP are introduced. The FMP overhang structure is made of SMC to allow more axial flux. Detailed comparisons indicate that the proposed machine can effectively utilize the end winding space to enhance the air-gap flux density and offer higher torque density than the conventional machines with no overhang structure and only rotor overhang structure. Nevertheless, the efficiency of the proposed machine is slightly sacrificed due to the use of SMC.

Author Contributions: Conceptualization, D.Y. and X.H.; methodology, D.Y. and L.W.; software, D.Y. and X.H.; formal analysis, D.Y. and L.W.; data curation, D.Y. and Y.F.; writing, D.Y. and X.H.; supervision, L.W. and Y.F.; funding acquisition, X.H. and Y.F.

Funding: This work was supported by the National Natural Science Foundation of China under Grant 51877196, 51637009, Ningbo Innovation 2020 program, and the Cao Guangbiao High Tech Development Fund of Zhejiang University.

Conflicts of Interest: The authors declare that there is no conflict of interest.

References

- Lee, C.H. Vernier motor and its design. *IEEE Trans. Power Appl. Syst.* **1963**, *82*, 343–349. [[CrossRef](#)]
- Toba, A.; Lipo, T.A. Generic torque-maximizing design methodology of surface permanent-magnet vernier machine. *IEEE Trans. Ind. Appl.* **2000**, *36*, 1539–1546.
- Gu, C.; Zhao, W.; Zhang, B. Simplified Minimum Copper Loss Remedial Control of a Five-Phase Fault-Tolerant Permanent-Magnet Vernier Machine under Short-Circuit Fault. *Energies* **2016**, *9*, 860. [[CrossRef](#)]
- Kim, B.; Lipo, T.A. Operation and Design Principles of a PM Vernier Motor. *IEEE Trans. Ind. Appl.* **2014**, *6*, 3656–3663. [[CrossRef](#)]
- Kim, B.; Lipo, T.A. Analysis of a PM vernier motor with spoke structure. *IEEE Trans. Ind. Appl.* **2016**, *52*, 217–225. [[CrossRef](#)]
- Jang, D.; Chang, J. A Novel Design Method for the Geometric Shapes of Flux Modulation Poles in the Surface-Mounted Permanent Magnet Vernier Machines. *Energies* **2017**, *10*, 1551. [[CrossRef](#)]
- Zhang, Y.; Lin, H.; Fang, S.; Huang, Y.; Yang, H.; Wang, D. Air-gap flux density characteristics comparison and analysis of permanent magnet vernier machines with different rotor topologies. *IEEE Trans. Appl. Supercond.* **2016**, *26*, 1–5. [[CrossRef](#)]

8. Li, D.; Qu, R.; Lipo, T.A. High-power-factor vernier permanent-magnet machines. *IEEE Trans. Ind. Appl.* **2014**, *50*, 3664–3674. [[CrossRef](#)]
9. Li, X.; Chau, K.T.; Cheng, M. Comparative analysis and experimental verification of an effective permanent-magnet vernier machine. *IEEE Trans. Magn.* **2015**, *51*, 1–9.
10. Liu, G.; Chen, M.; Zhao, W.; Chen, Q.; Zhao, W. Design and analysis of five-phase fault-tolerant interior permanent-magnet Vernier machine. *IEEE Trans. Appl. Supercond.* **2016**, *26*, 1–5. [[CrossRef](#)]
11. Yang, H.; Lin, H.; Zhu, Z.-Q.; Fang, S.; Huang, Y. A Dual-Consequent-Pole Vernier Memory Machine. *Energies* **2016**, *9*, 134. [[CrossRef](#)]
12. Oner, Y.; Zhu, Z.Q.; Wu, L.J.; Ge, X.; Zhan, H.; Chen, J.T. Analytical on-load subdomain field model of permanent-magnet vernier machines. *IEEE Trans. Ind. Electron.* **2016**, *63*, 4105–4117. [[CrossRef](#)]
13. Liu, X.; Zhong, X.; Du, Y.; Chen, X.; Wang, D.; Ching, T.W. A New Magnetic Field Modulation Type of Brushless Double-Fed Machine. *IEEE Trans. Appl. Supercond.* **2018**, *28*, 1–5. [[CrossRef](#)]
14. Xu, L.; Liu, G.; Zhao, W.; Yang, X.; Cheng, R. Hybrid stator design of fault-tolerant permanent-magnet vernier machines for direct-drive applications. *IEEE Trans. Ind. Electron.* **2017**, *64*, 179–190. [[CrossRef](#)]
15. Seo, J.M.; Jung, I.S.; Jung, H.K.; Ro, J.S. Analysis of overhang effect for a surface-mounted permanent magnet machine using a lumped magnetic circuit model. *IEEE Trans. Magn.* **2014**, *50*, 1–7.
16. Yeo, H.K.; Park, H.J.; Seo, J.M.; Jung, S.Y.; Ro, J.S.; Jung, H.K. Electromagnetic and thermal analysis of a surface-mounted permanent-magnet motor with overhang structure. *IEEE Trans. Magn.* **2017**, *53*, 1–4. [[CrossRef](#)]
17. Min, S.G.; Bobba, D.; Sarlioglu, B. Analysis of overhang effects using conductor separation method in coreless-type PM linear machines. *IEEE Trans. Magn.* **2018**, *54*, 1–4. [[CrossRef](#)]
18. Ishikawa, T.; Sato, Y.; Kurita, N. Performance of novel permanent magnet synchronous machines made of soft magnetic composite core. *IEEE Trans. Magn.* **2014**, *50*, 1–4. [[CrossRef](#)]
19. Wn, F.; El-Refaie, A.M. Permanent magnet vernier machine: A review. *IET Electr. Power Appl.* **2019**, *13*, 127–137.
20. Okada, K.; Niguchi, N.; Hirata, K. Analysis of a Vernier Motor with Concentrated Windings. *IEEE Trans. Magn.* **2013**, *49*, 2241–2244. [[CrossRef](#)]



© 2019 by the authors. Licensee MDPI, Basel, Switzerland. This article is an open access article distributed under the terms and conditions of the Creative Commons Attribution (CC BY) license (<http://creativecommons.org/licenses/by/4.0/>).